Review of Scientific Instruments

Endstation for ultrafast magnetic scattering experiments at the free-electron laser in Hamburg

Cite as: Rev. Sci. Instrum. **84**, 013906 (2013); https://doi.org/10.1063/1.4773543
Submitted: 20 July 2012 • Accepted: 11 December 2012 • Published Online: 24 January 2013

L. Müller, C. Gutt, S. Streit-Nierobisch, et al.

Endstation for ultrafast magnetic scattering experiments at the free-electron laser in Hamburg

L. Müller,[1] C. Gutt,[1] S. Streit-Nierobisch,[1] M. Walther,[1] S. Schaffert,[2] B. Pfau,[2] J. Geilhufe,[2,3] F. Büttner,[2,4,a)] S. Flewett,[2,b)] C. M. Günther,[3] S. Eisebitt,[2,3] A. Kobs,[5] M. Hille,[5] D. Stickler,[5] R. Frömter,[5] H. P. Oepen,[5] J. Lüning,[6] and G. Grübel[1]
[1]*Deutsches Elektronen-Synchrotron DESY, 22607 Hamburg, Germany*
[2]*Technische Universität Berlin, 10623 Berlin, Germany*
[3]*Helmholtz-Zentrum Berlin für Materialien und Energie GmbH, 14109 Berlin, Germany*
[4]*Paul Scherrer Institut, 5232 Villigen PSI, Switzerland and École Polytechnique Fédérale de Lausanne, 1015 Lausanne, Switzerland*
[5]*Universität Hamburg, 20355 Hamburg, Germany*
[6]*Université Pierre et Marie Curie, 75231 Paris, France*

(Received 20 July 2012; accepted 11 December 2012; published online 24 January 2013)

An endstation for pump–probe small-angle X-ray scattering (SAXS) experiments at the free-electron laser in Hamburg (FLASH) is presented. The endstation houses a solid-state absorber, optical incoupling for pump–probe experiments, time zero measurement, sample chamber, and detection unit. It can be used at all FLASH beamlines in the whole photon energy range offered by FLASH. The capabilities of the setup are demonstrated by showing the results of resonant magnetic SAXS measurements on cobalt-platinum multilayer samples grown on freestanding Si_3N_4 membranes and pump-laser-induced grid structures in multilayer samples. © *2013 American Institute of Physics*. [http://dx.doi.org/10.1063/1.4773543]

I. INTRODUCTION

Understanding ultrafast magnetization dynamics on the nanoscale is a challenging problem in modern magnetism research with direct impact on the quest for faster and smaller storage devices. Probing the magnetization element-specifically and on the nanometer lengthscale is a prerequisite when studying technologically relevant systems with their complex compositions.

In a pioneering experiment in 1996, it was discovered by Beaurepaire and co-workers[1] that the magnetization in a ferromagnet can be quenched by an ultrashort laser pulse within a few hundred femtoseconds. Since then, many studies supported this so-called ultrafast demagnetization, see, e.g., Refs. 2–5. However, all these studies address either (using the magneto-optic Kerr effect) the net-magnetization of a homogeneously magnetized sample with a spatial resolution of about 1 μm at best,[6] or (using X-rays from femtoslicing sources[7]) the magnetization of a homogeneously magnetized sample in an element-selective way.[8–11]

While those measurements address magnetization dynamics down to the sub-100 fs scale, spatial information on the nanometer lengthscale is not accessible due to wavelength or flux limitations, respectively. High-quality scattering or imaging experiments are, however, possible – though without the desired time resolution – at "standard" synchrotron radiation sources via scanning transmission X-ray microscopy[12] or Fourier transform X-ray holography, which also offers a microscopy mode.[13–15]

With the advent of vacuum ultraviolet (VUV) and X-ray free-electron lasers (FEL) with their high peak brilliance and short pulse lengths in the 100 fs range it becomes possible for the first time to access the ultrafast time and the nanometer lengthscales simultaneously. Pioneering experiments showing the feasibility of single- as well as multi-shot experiments at FEL sources were performed on cobalt-platinum multilayer samples at the *M*- and *L*-edges of cobalt.[16,17]

Experiments at FEL sources require specialized experimental stations tailored to the scientific problem. Here, we describe a flexible small-angle X-ray scattering (SAXS) endstation that can be used at any FLASH beamline for pump–probe experiments. The general layout of such experiments is sketched in Fig. 1. The setup was so far used for resonant magnetic scattering measurements at the *M*-edges of cobalt and for a standard scattering experiment, i.e., scattering from charge inhomogeneities, at the same energy.

At the FERMI@ELETTRA FEL one beamline is dedicated to diffraction and projection imaging. The local endstation[18] will offer similar measurement possibilities and, as a permanent endstation, is well integrated in the beamline. The linac coherent light source at SLAC offers a beamline dedicated to soft X-rays with an energy range from 480 eV up to 2 keV for which also an endstation for pump–probe type scattering and imaging experiments exists.[19] With its different energy range this endstation can be seen as complementary to the endstation described here. At this beamline resonant X-ray holography of magnetic systems at FELs was pioneered recently.[20]

[a)]Additional present address: Johannes Gutenberg-Universität Mainz, 55099 Mainz, Germany.
[b)]Present address: Paul Scherrer Institut, 5232 Villigen PSI, Switzerland.

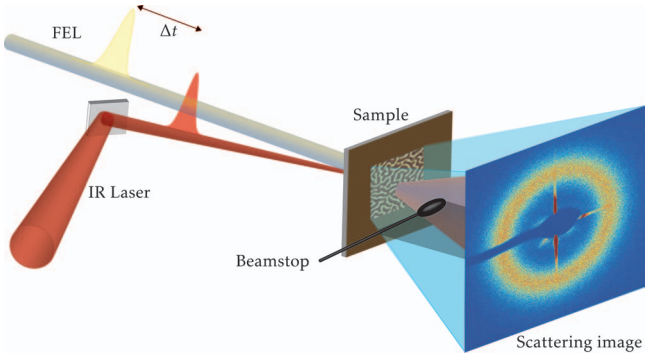

FIG. 1. Layout of a two-color pump–probe experiment at FLASH. The FEL and IR laser pulses hit the sample with an adjustable time delay Δt. A sample (shown is a $4 \times 4\ \mu m^2$ area of a magnetic multilayer sample imaged by magnetic force microscopy) produces small-angle scattering, which is detected by a CCD camera.

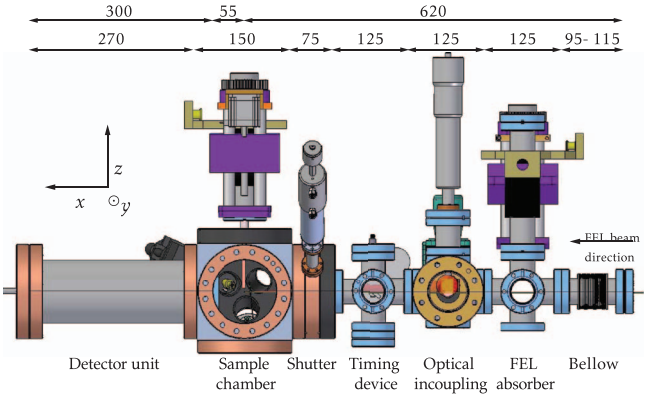

FIG. 2. Schematic of the SAXS setup for use at FLASH beamlines BL2 and BL3. The FEL beam direction is along the x direction and the IR laser beam enters along negative y direction. For clarity, the turbo pump attached at the bottom of the sample chamber, the vacuum gauge attached to the timing cross, and the x and y motors for the absorber and sample translators are omitted. Dimensions are given in millimeters. The measures denote the lengths of the components (lower) and (upper) the distance of the sample from the FEL exit-flange as well as the sample–detector distance. See Fig. 3 and text for details.

II. EXPERIMENTAL SETUP

The free-electron laser source FLASH in Hamburg provides linearly polarized, ultrashort light pulses with a duration between ≈30 fs and 300 fs in the VUV to soft X-ray regime. Wavelengths in the range from 4.45 nm up to 47 nm are available in the fundamental of the undulator.[21] FLASH offers 5 different beamlines, of which only one receives the FEL beam at any given time. Beamlines PG1 and PG2 use high-resolution grating monochromators to deliver bandwidths narrower than the native $\Delta\lambda/\lambda \approx 1\%$ delivered by FLASH,[22] or allow to select higher harmonics for the experiment.[23] Beamlines BL1–BL3, in contrast, do not use monochromators. Higher harmonics are suppressed by using carbon coated mirrors.[24] An infrared (IR) pump laser is available at all BL beamlines and at PG2. All FLASH beamlines allow the dedicated user-provided experimental chamber to be connected by a standardized CF flange. Further details on the FLASH facility and the beamlines can be found in Refs. 24, 25, and 26 and references therein.

All experimental endstations used at FLASH are installed only temporarily at the assigned beamline. Therefore, any setup has to be either easy to assemble at the beamline or transportable in its working configuration.

For the SAXS setup we designed a chamber that is transportable in its working configuration (Figs. 2–4). For the design the following requirements were taken into account:

- UHV compatibility – A pressure lower than 10^{-6} mbar is required for any experiment
- Compatibility with all FLASH beamlines and the vacuum-interlock system
- Compatibility with different laser incoupling arrangements
- Upgrade compatibility
- Device to measure the time delay between IR and FEL pulses
- Fast sample exchange
- Precise and reproducible sample positioning
- In-vacuum area detector for short sample–detector distances of only a few centimeters.

The chamber is mounted on top of a movable base frame. Fine alignment is achieved via the motorized T-shaped pedestal of the base frame offering a travel of 70 mm in x, 180 mm in y, and 90 mm in z direction. Two independent actuators for the y and three for the z directions allow for tilt corrections around any chosen center of rotation. The maximum rotation angle is depending on the position of the point of rotation and is of the order of a few degrees when rotating around a point within the base frame.

The chamber is constructed with standard vacuum CF components to allow for flexible rearrangement. The different components are described in the following.

The first component (in FEL beam direction) is a solid-state absorber. It is housed in the first double-cross (CF40) and consists of absorber foils which can be changed by a three-axes translator offering 100 mm travel perpendicular to the FEL beam in z direction. The other two axes offer 25 mm of travel in x and y directions and are used for initial alignment of the foils (Figs. 2 and 3). The absorber is used mainly for alignment purposes to adjust the FEL fluence to a level at which no damage is induced in the sample or detector. The absorbers for 60 eV are listed in Table I.

The following double-cross (CF40/CF63) houses the optical incoupling unit. The IR laser is externally reflected upwards by a periscope equipped with two 2 in. diameter silver mirrors to match the 200 mm beam height difference between FEL and IR laser (Fig. 4). A 600 mm focal length fused-silica lens is used to focus the IR beam onto the sample. The lens can be translated over 150 mm in beam direction to match the IR beamsize to the FEL beamsize at the sample position. The IR beam is then coupled into the chamber through a high-quality fused-silica window (CF63) and reflected onto the sample by a rectangular metal mirror (Fig. 3). Spatial overlap of both beams at the sample position is achieved by manually moving the IR laser position using the angle-adjustment screws of the mirror mounts at the periscope. Both lasers can be observed in the sample plane by a fluorescent screen made

TABLE I. Aluminum absorber thicknesses used for a photon energy of ≈60 eV. The absorbers have an opening of 3 mm in diameter. Values are calculated from data in Ref. 27

Absorber no.	Thickness (μm)	Transmission at 60 eV
1	10	8.0×10^{-7}
2	8	1.3×10^{-5}
3	6	2.2×10^{-4}
4	3	1.5×10^{-2}
5	2	6.0×10^{-2}

of microscopic YAG crystals, painted onto a small piece of steel (Fig. 5). The FEL beam passes approximately 5 mm below the mirror so that both beams are quasi-collinear with an angular deviation of $<3^\circ$.

The third cross (CF40) houses the timing device to establish the temporal overlap of IR and FEL pulses. A grid of gold wires can be moved into the beam by a manual translation and rotation stage. The grid scatters both types of radiation, which are then detected by a fast photodiode (200 ps rise time, IRD AXUVHS11) (Fig. 3). The signal of the photodiode is visualized by a fast oscilloscope and by changing the optical path length of the IR laser both peaks are moved to the same position relative to a trigger signal.[28] Using this procedure both pulses can be synchronized well within ±50 ps. Fine adjustment is established by observing the response of the magnetic scattering signal to pumping. The rough timing procedure via the photodiode is usually done only once at the beginning of the experiment. The timing, once established, is stable apart from a slow drift of usually 1 ps/h which can be monitored via FLASH diagnostic equipment during the experiment.[26]

The adapter piece from the CF40 flange to the CF100 sample chamber houses a manual pneumatic shutter to protect

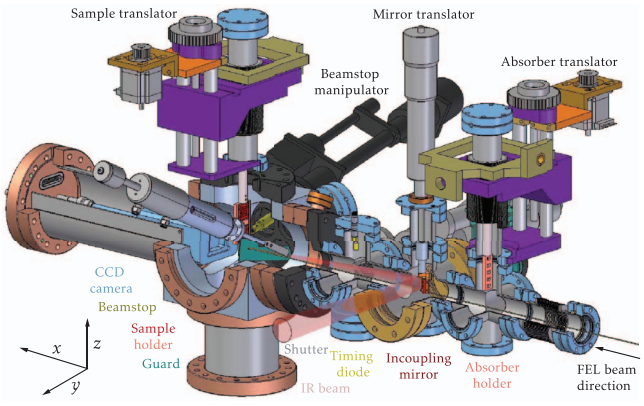

FIG. 3. Schematic of the chamber. The FLASH beam (fine line) enters from the lower right in x direction and the IR-Laser, represented by the red cone enters from the front. In FEL beam direction the first cross contains the solid-state absorbers (Table I). The second cross houses a metal mirror to reflect the IR laser beam quasi-collinearly to the FEL beam onto the sample. The third cross contains the timing device and the vacuum gauge (not shown for clarity). The following adapter part contains a pneumatic shutter to protect the CCD camera during timing measurements and general alignment. The sample chamber (CF100 cube) contains besides the sample holder a guard hole and the beamstop. The following tube houses the CCD camera. Its chip is positioned 5.5 cm from the sample in the shown configuration. See text for details.

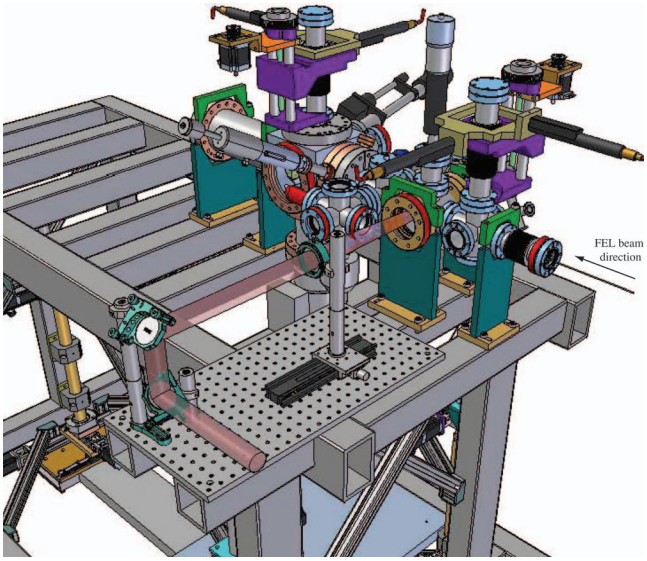

FIG. 4. Complete setup as used at BL3. Here, the chamber is shown mounted onto the base frame with all additional parts including the optical incoupling setup. See Figs. 2 and 3 to identify the various parts of the chamber.

the sample and the CCD camera from IR and FEL radiation during alignment and timing procedures.

The sample chamber consists of a CF100 cube and a CF40 3-axis translator attached to its top. The sample holder is attached to a holding rod mounted at the top flange of the translator. The translator offers 100 mm travel in z and 25 mm in x and y directions. The sample holder can accommodate two 23.5×23.5 mm^2 samples and a fluorescence screen; smaller samples are mounted via adapter plates (Fig. 5). In order to change samples, the carrier rod is taken out at the top flange of the translator to minimize eventual damage to parts inside the chamber.

An aperture with a diameter of 1.5 mm can be moved manually to a position a few millimeters in front of the sample to absorb FEL stray light which otherwise contaminates the scattering image. Behind the sample a linear-rotary feedthrough carries a beamstop made from a stretched silver-plated copper wire ($\varnothing < 0.5$ mm) with a drop of tin solder ($\varnothing \approx 1$ mm) at its end. The beamstop completely absorbs the high-intensity direct beam and prevents damage of the CCD detector.

Additionally, viewports allow to visually check the alignment of the sample. Direct observation of the sample and the

FIG. 5. Photograph of a sample holder with one multi-window sample (left), one adapter plate for smaller samples (right), and a fluorescence screen (center).

FEL or IR beam on a fluorescence screen is done via a long-distance microscope (field of view 1.6 mm– 20.3 mm depending on the zoom setting at a working distance of ≈33 cm).

Finally, the detector unit contains the CCD camera and provides feedthroughs for the necessary cooling water and signal cables. The electrical feedthrough is implemented using a standard Sub-D feedthrough and the water feedthrough uses vacuum compatible copper-sealed VCR® connections.

The CCD camera itself is an in-vacuum, Peltier-cooled soft X-ray CCD with 2048 × 2048 pixels resolution and a pixel size of 13.5 μm (Princeton Instruments, PiMte2048). It is mounted on a supporting L-shaped rod attached to the rear flange that also incorporates the feedthroughs. The sample-detector distance ℓ is adjustable in a few fixed steps by different lengths of CF100 tubes and distance parts. Typically, we used distances between $\ell = 55$ mm and 130 mm when working at around 60 eV (M-edge) and around $\ell = 600$ mm would be necessary when using 778 eV (Co L-edge) to fit the observed Q range to the typical domain size distributions in our samples.

The CCD camera is sensitive to soft X-ray radiation as well as to visible light and IR radiation. Therefore, the pump-laser radiation and other optical stray light has to be blocked by a filter. Here, a free standing, 250 nm thick aluminum filter with an opening of 32 × 32 mm^2 glued on an aluminum support is mounted directly onto the camera head, approximately 5 mm from the CCD chip. The filter has a transmission of 70% at 60 eV while it totally blocks visible and IR radiation. The volume between chip and filter is evacuated via the camera's venting valve and two venting grooves cut into the filter support. The grooves are meander shaped to prevent the transmission of straylight. An alternative filter type uses 100 nm thick aluminum supported by a nickel mesh. This filter offers higher overall transmission of ≈86% at 60 eV but with the drawback of shadowing by the mesh superimposed onto the image. Due to the transmission behavior of aluminum these filters can be used at energies from 20 eV– 70 eV and at energies higher than 400 eV where the transmission becomes better than ≈50% of the value at 60 eV again.

At the bottom of the sample chamber a CF100 turbo pump with a pumping speed of 260 l/s is attached to evacuate the chamber to a pressure $p_m < 6 \times 10^{-6}$ mbar that is needed before the valves may be opened to the FLASH beamline.

Evacuating the chamber down to a pressure of around 10 mbar has to be done slowly as the volume between CCD chip and filter is evacuated through rather small slits and the filter itself can only withstand small pressure differences. Pumping speeds of 10 mbar/s have so far proven safe. Once a pressure of ≈ 10 mbar is reached, the chamber can be evacuated to p_m within 10 min even if the CCD camera is switched on and is already cooling. The minimum pressure reachable with the CCD camera switched on is ≈5 × 10^{-7} mbar. With this fast pumping, samples can be changed within less than an hour where most time is used to warm up the CCD camera prior to venting to prevent condensation on the chip.

The 800 nm femtosecond pump-laser beam is supplied by the FLASH facility and its detailed setup is described in Ref. 26. In our case, we used a Hydra amplifier delivering sub 100 fs pulses with an energy of up to 1 mJ at the experiment. The beam diameter is about 20 mm after the exit flange of the laser beamline. The pulses are available at a frequency of 10 Hz and are electronically synchronized to the soft X-ray pulses from FLASH. The temporal jitter is on the order of 300 fs; different devices to measure the jitter on a shot-by-shot basis are now available.[26,29,30]

The setup can be used for single- and multi-shot pump–probe experiments. While single-shot experiments yield the highest time resolution only limited by the accuracy of the jitter determination, multi-shot exposures offer improved counting statistics which is limited only by the number of shots averaged. The time resolution in this case is governed by the synchronization jitter. Aside from the high time resolution in single-shot operation mode, high pump fluences, which alter the sample irreversibly can be explored.

III. APPLICATION EXAMPLES

A. Pump–probe resonant magnetic small-angle X-ray scattering

SAXS allows to measure structures in a sample on a sub-micrometer lengthscale depending on the observed Q-range.[31] We use specially prepared samples with out-of-plane magnetic anisotropy with a typical domain size of 100 nm. This magnetic structure is probed by tuning the photon energy to the Co $M_{2,3}$ absorption edge such that the scattering is sensitive to the different population of electronic states of cobalt in domains of opposite magnetization direction.

The resonant magnetic scattering amplitude f can be expressed for each lattice site by[32]

$$f = (\mathbf{e}' \cdot \mathbf{e})F_c - i(\mathbf{e}' \times \mathbf{e})\mathbf{M}F_{m_1} + (\mathbf{e}' \cdot \mathbf{M})(\mathbf{e} \cdot \mathbf{M})F_{m_2}, \quad (1)$$

where $\mathbf{e}$ and $\mathbf{e}'$ represent the polarization unit vectors of the incident and scattered waves, respectively, $\mathbf{M}$ denotes the sample magnetization, and F the resonant scattering amplitudes for charge (F_c) and magnetic (F_m) scattering. While F_{m_1} describes scattering within the framework of the X-ray magnetic circular dichroism (XMCD) effect,[33–36] the third term in Eq. (1) describes the scattering due to linear magnetic dicroism. This term is zero in the here presented case as the sample's magnetization and the incident X-ray polarization directions are perpendicular. Therefore, only the second term contributes to the magnetic scattering.

FLASH delivers horizontally polarized radiation. After the scattering process, the magnetically scattered radiation has vertical polarization, whereas the charge scattered radiation remains horizontally polarized, such that both wave fields cannot interfere at the detector.[37] Generally, the total intensity measured on the detector is given by

$$I(\mathbf{Q}) \propto \left| \sum_j f_j \cdot \exp(i\mathbf{Q} \cdot \mathbf{r}_j) \right|^2. \quad (2)$$

Here, $\mathbf{Q}$ denotes the wave-vector transfer, $\mathbf{r}_j$ the position of the jth atom, and f_j the scattering amplitude from Eq. (1). In the special case of linearly polarized radiation combining both equations leads to

$$I(\mathbf{Q}) \propto \left|\tilde{F}_c(\mathbf{Q})\right|^2 + \left|\tilde{M}_1(\mathbf{Q})\right|^2 \quad (3)$$

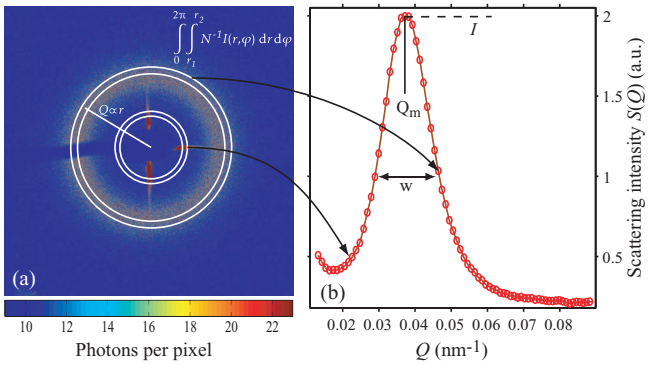

FIG. 6. Magnetic scattering image from a cobalt/platinum multilayer sample as described in the text. For the exposure, 3 single FEL shots were summed at low repetition rate (1 Hz) and no pump laser was used. Quantitative analysis is done by radial integration after masking the beamstop and charge scattering areas as indicated. From the resulting $S(Q)$ distribution real space parameters of the magnetic system can be extracted. See text for details.

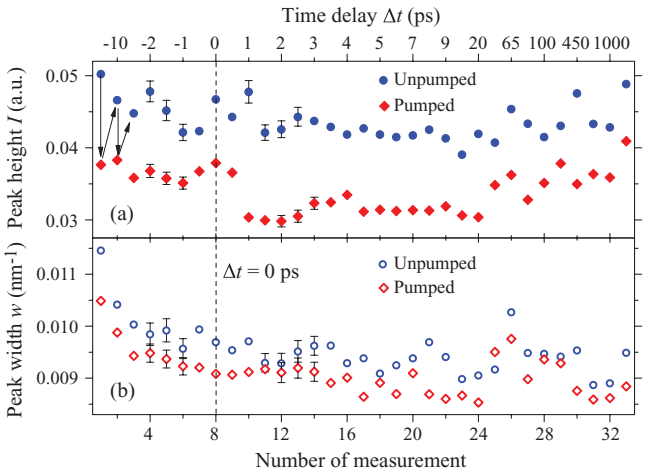

FIG. 7. Results from a pump–probe experiment with interleaved unpumped references measurements averaging 100 FEL shots at a repetition rate of 10 Hz for each data point. Evaluation has been done according to Fig. 6 and some typical error bars are given. Unpumped reference and pumped data have been taken in alternating order and with increasing delay time (top axis) as indicated by arrows in (a). In terms of the dynamics in question negative delay times imply an effectively unpumped sample, as the probe pulse impinges on the sample before the pump pulse. Even at negative time delay a clear difference in the scattering peak intensity I is observed. This can only be explained by a static heating effect due to the repeated energy deposition by both, the pump and probe pulses. (b) The peak width w undergoes an ageing effect particularly during the first 4 measurements, i.e., the domain-width distribution becomes narrower. See text for details.

with the electron density structure factor $\tilde{F}_c$ and the magnetic structure factor $\tilde{M}_1$ being the Fourier transforms of F_c and $M F_{m_1}$, respectively, which relate the real-space structure to the scattering image.

In the case of XUV SAXS discussed here, the sample thickness is severely limited due to the strong absorption. As the absorption of any material varies strongly with the photon energy, the optimum sample thickness has to be determined for each sample separately but is likely to be in the range from a few tens up to hundreds of nanometers. For our samples, we typically use free-standing 50 nm thick Si_3N_4 membranes as substrate with a transmission of ≈37% at a beam energy of ≈60 eV corresponding to the M-edge of cobalt and for the multilayer films typically a total platinum thickness of ≈23 nm and ≈13 nm of cobalt. Including the substrate the samples transmit about 1% of the radiation.

In detail, the samples used are ferromagnetic $(Co_{0.8nm}Pt_{1.4nm})_{16}$ multilayer films with an out-of-plane magnetic anisotropy grown via electron-cyclotron and direct-current magnetron sputtering on a Si_3N_4 membrane. The membrane window size is $250 \times 250\,\mu m^2$. Details of the growth process are published in Refs. 38 and 39. The lengthscales of charge inhomogeneities are different from those of the magnetic domain structure due to the growth process, so that charge and magnetic scattering intensities appear well separated in the scattering image.[13,40,41] Thus, the observed scattering ring can be seen as purely magnetic and the observed intensities I are a measure of the magnetization via $M \propto \sqrt{I}$. These kinds of samples have also been used in proof-of-principle experiments.[17] After the deposition process, the samples can be treated magnetically to exhibit either an isotropic worm domain pattern or a partially ordered stripe domain phase. This is achieved by out-of-plane demagnetization or in-plane magnetization, respectively. All data shown here are taken from samples in the worm domain phase, which is close to equilibrium. Accordingly, an isotropic scattering ring is observed (Fig. 6(a)).

As detailed above, the sample magnetization can be followed in scattering experiments via observation of the intensity of the magnetic scattering image, while the position of the peak in Q-space is a measure of the average domain width. Additionally, in coherent mode changes in the speckle pattern are accessible.[42,43]

The Q dependent strength of the scattering signal is extracted from the CCD data via radial integration around the center position (Fig. 6). The beamstop region and the high-intensity streaks from scattering of the membrane-window edges are masked beforehand so that data at $Q \leq 0.013\,nm^{-1}$ are not available. From $S(Q)$ the strength I of the magnetic scattering, the average domain widths l and the distribution of the domain widths w can be extracted.

The intense IR and FEL radiation deposits a considerable amount of heat in the sample. While this is not an issue for single-shot mode in multi-shot experiments the heating effect might interfere with the measurement and, therefore, has to be measured or minimized. In a multishot experiment, i.e., when many FEL shots are averaged in one CCD exposure, at the maximum repetition frequency (10 Hz) of FLASH a static heating effect due to energy deposition in the system is observed in addition to the ultrafast demagnetization process (Fig. 7(a)). The repeated energy deposition in the sample by the IR and FEL light pulses heats up the sample system leading to a smaller magnetization M and consequently to a smaller peak intensity I. The heating effect from the IR laser becomes obvious at negative delay times and overlays with the decrease of I, induced by ultrafast demagnetization at positive delay times. Heating due to the FEL pulses alone cannot be quantified by the data. However, the amount of energy deposition of FEL and IR radiation is similar and, therefore, it can be presumed that their effect on heating and hence

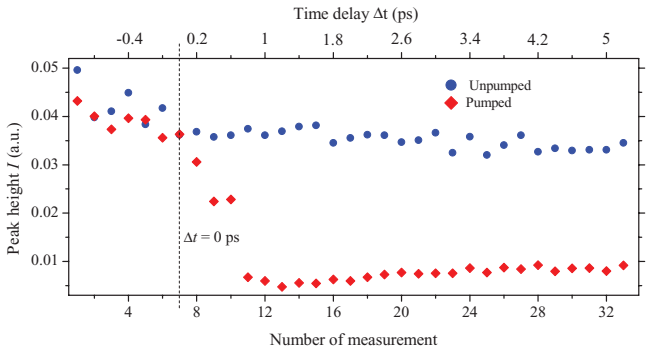

FIG. 8. At a reduced repetition frequency of 1 Hz, the heating effect observed when using the full repetition rate of 10 Hz (Fig. 7(a)) is no longer significant. Data points have also been taken in an alternating unpumped/pumped order.

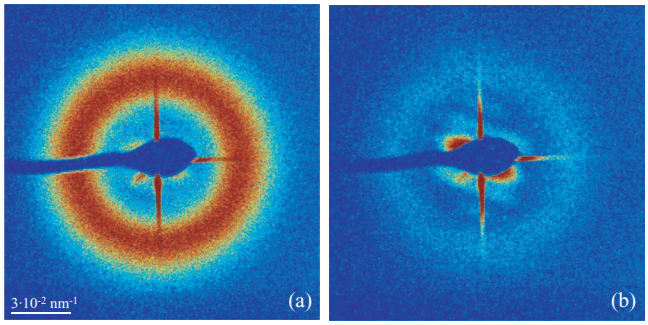

FIG. 9. Magnetic scattering data from the same sample in (a) unpumped and (b) pumped condition. The delay time between pump and probe laser was set to 1.2 ps and the pump fluence was 18 mJ/cm^2. In both cases, three FEL shots were averaged at 1 Hz repetition rate to minimize the heating effect (Fig. 7). Speckles cannot be resolved due to the large illuminated area and the short sample-detector distance.

diminishing of the scattering signal are of similar magnitude. As each data point represents an average over 100 shots with high repetition rate, the base temperature of the sample rises continuously and it is hence not possible to relate the change in the magnetic scattering to a temperature change of the magnetic film.

All single measurements shown in Fig. 7 are done on the same sample being not irradiated by XUV or IR radiation beforehand and the delay time Δt was increased monotonically. Therefore, a possible aging of the sample due to the irradiation can be observed. For the peak intensity I in the unpumped case no systematic change can be observed. This implies that the multi-layer system as such stays intact for the here used small fluences. The increased scattering of the data from measurement number 23 on points towards an aging of other than magnetic parameters of the sample. The sample is strongly heated by each IR and FEL pulse[17] transiently and in this case also statically so that a change of elastic parameters, e.g., due to recrystallization, is expected. This leads, after a certain point, to a change in details of the sample's waviness which influences the scattering intensities. Apart from that, in the pumped case the development of the intensity follows qualitatively the expectations for a demagnetization experiment. When looking at the width of the scattering peak (Fig. 7(b)) a clear evolution towards a more narrow scattering ring is observed. This is due to the fact that the domain system is not completely in its equilibrium configuration at the beginning of the experiment and, therefore, a broader domain-width distribution exists. Being exposed to the radiation domain-wall depinning processes are triggered, the system is driven towards the equilibrium distribution and, therefore, the domain-width distribution narrows. Note further that a small difference in w exists for the pumped and unpumped case.

For the final experiment, the heating effect has been minimized by reducing the FEL and IR laser repetition rates to 1 Hz (Fig. 8). The reduced heating leads effectively to a larger difference in the scattering strengths of the pumped and unpumped sample, respectively, and allows to follow unambiguously the ultrafast demagnetization as a function of delay time and flux. Furthermore, with the reduced mean temperature during the exposure it can be expected that the sample can withstand a greater number of measurements as interdiffusion in the layer system is reduced.

When pumping the sample with the IR laser hence a clear decrease of the magnetic scattering intensity can be observed as expected for ultrafast demagnetization (Fig. 9). The taken data show the pump flux dependence of ultrafast demagnetization (Fig. 10). Fits with an exponential form (see, e.g., Refs. 44 and 45),

$$I = \Theta(t) \cdot \left\{ A \cdot \left[1 - \exp\left(-\frac{t}{t_{ee}} \right) \right] \cdot \exp\left(-\frac{t}{t_{ep}} \right) + B \cdot \left[1 - \exp\left(-\frac{t}{t_{ep}} \right) \right] \right\} \cdot \exp\left(-\frac{t}{t_{th}} \right) + C \quad (4)$$

yield timescales for the demagnetization in the range of $t_{ee} = (240 \pm 50)$ fs in accordance with literature, see e.g., Ref. 46. Here, $\Theta(t)$ denotes the Heaviside step function with $\Theta(t) = 0$ if $t < 0$ and $\Theta = 1$ for $t > 0$. The variables t_{ee} denotes

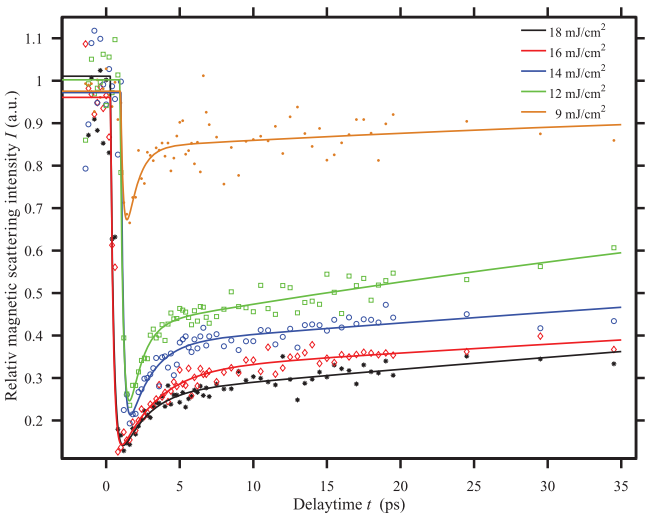

FIG. 10. Pump flux dependent ultrafast demagnetization measured at FLASH. The height of the magnetic scattering peak has been determined by radial integration over the CCD images (Fig. 9) each of which in an average over three FEL shots. The solid lines represent fits using Eq. (4). The shift in time zero of about 1 ps between the measurements is caused by the drift in the synchronization of FLASH (see Sec. II). The momentary value of time zero has been accounted for while fitting via a simple shift in t.

the electron–electron thermalization time, t_{ep} the electron–phonon relaxation time, and t_{th} describes the "long term" thermal relaxation rate (i.e., heat diffusion out of the irradiated area) of the sample. A describes the amount of demagnetization and B the recovery of the magnetization, whereas C describes the constant magnetization at times $t < 0$ s and is equal to 1 within the error due to the normalization. For the timescale t_{ep} a value between 1 ps and 2 ps can be determined; t_{th} cannot be determined reliably as it is several times longer than the maximum set delay time. Aside from the demagnetization timescale the scattering data can be analyzed with respect to spatial changes in the domain pattern giving insight into the physics of ultrafast demagnetization.[47]

B. High pump-laser fluence induced grid structures

FEL sources allow to take data with a single ultrashort pulse which allows to study, e.g., transient states. An example is the use of high pump powers that on their own destroy or alter the sample permanently as, e.g., melting or recrystallization.

One example for such a process are femtosecond-laser-induced modifications of glasses[48–50] or semiconductors.[51] The use of FELs to studies such phenomena will allow deeper insight into their dynamics at short timescales and at spatial lengthscales smaller than accessible with other techniques.

In our experiment, using the same sample system as described in Sec. III A, we increase the power of the IR pump laser to about 120 mJ/cm^2 and set a time delay of 400 ps keeping all other parameters unchanged. With these settings the magnetization remains quenched upon arrival of the probe pulse and no magnetic signal is expected to be measured even though the measurement is done at the cobalt resonance. However, transient or permanent structures induced in the sample by the high-intensity pump laser can be studied.

Here, modifications ordered in a grid are induced in the sample system before it is destroyed by the high fluence of the FEL used in this experiment. This grid translates to a corresponding grid structure in the scattering image (Figs. 11(a)–11(c)). We assume that shining the pump laser from the etch-pit side directly onto the dielectric silicon nitride membrane (Fig. 11(d)) leads, via reflection from the bevels, to a modulation of the laser intensity distribution on the sample due to interference. The scattering contrast arises from the different electron density of the fraction of material that was modified in the intensity maxima of the IR-laser as the magnetization is quenched by the pump laser. From the condition for formation of interference maxima $\sin\alpha_n = n \cdot \lambda \cdot d^{-1}$, we conclude that the characteristic lengthscale d between the modified areas is (790 ± 15) nm, which is compatible with the IR wavelength. In this experiment, only the spacing of the single modifications can be determined, whereas the atomic structure within each modified area is not accessible due to the long wavelength of the FEL radiation. However, with the now upcoming hard X-ray FELs it will be possible to resolve atomic dynamics during the modification process, which is otherwise inaccessible. The feasibility of such experiments has been demonstrated in a pioneering experiment by Lindenberg *et al.*[52]

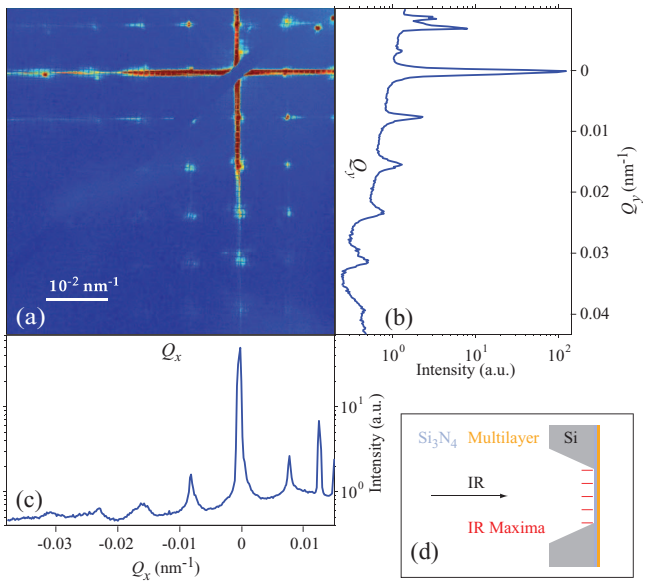

FIG. 11. CCD image (a) and line integration along the Q_x and Q_y directions (b) and (c) for a strongly pumped sample (120 mJ cm^{-2} not taking into account the lateral variation of the intensity). The structured pump laser has induced changes in the sample which are aligned in a grid. Therefore, the scattering also shows a grid-like structure and the periodicity yields the pump laser's wavelength. The high-intensity streaks intersecting at $Q = 0$ nm^{-1} are scattering from the membrane window. At higher magnification, fine dark lines become visible which are an artefact from the Ni mesh supporting the aluminum filter used in this experiment. See text for details. (d) The sample is irradiated from the groove side such that the pump-laser radiation is structured on the sample surface.

IV. SUMMARY AND OUTLOOK

We have designed a modular endstation suitable for the FLASH beamlines containing all key components, absorber, optical incoupling, time-zero measurement, sample chamber, beamstop, and detection unit. The chamber allows for pump–probe measurements in standard SAXS geometry in the whole photon energy range offered by FLASH.

We have successfully used the chamber to pioneer magnetic scattering at FEL sources[16,17] and to measure the spatial response of a cobalt-platinum multilayer system in a multi-domain state during ultrafast demagnetization induced by an IR laser pulse.[47] Furthermore, the intra-pulse interaction of a high intensity FEL pulse with the magnetic system could be probed.[53] The experimental scheme provides access to the ultrafast dynamics of the magnetic domain system with spatial resolution on the nanoscale in an element-selective way. Furthermore, material modifications induced by a single high-intensity IR pulse were observed.

Improvements will be made concerning the setup itself and its incorporation into the FLASH system. The CCD camera will be mounted movable for easy adjustment of the observable Q range and also the sample position will be made variable with respect to the FEL focus so that the beam size and therewith the fluence level on the sample can be set.

The ultimate goal of imaging magnetic domains during the demagnetization process will be tackled in future experiments. One of the most promising approaches – Fourier transform holography[13] – however requires circularly or at least elliptically polarized X-rays, which are at present not

available at FLASH. Furthermore, the use of X-rays at the *L*-edge is preferable due to the higher spatial resolution. To this end, a transmission polarizer for the *L*-edges of the transition metals is under development[54] which can be used at FLASH beamlines adapted to higher energies in the range of 700 eV–800 eV. These kinds of polarizers employ the XMCD effect having different transmissions for left- and right-circularly polarized portions of the linearly polarized X-rays so that ≈60% of circular polarization can be obtained at a transmission of a few percent. This presents a good trade-off between degree of polarization and intensity.

The ongoing upgrades of FLASH, especially the FLASH II project, will lead to easier access to these higher photon energies in the range of 800 eV. In addition, the possibility to deliver variable linear and circular polarization directly from the machine via a so-called "afterburner" in form of an APPLE III undulator[55] is under discussion. Together with the seeding then available for the FEL new ambitious experiments can be performed. The, via seeding, perfect synchronization to the pump laser and the complete circular polarization of the FEL beam will allow for combined ultimate-time-resolution pump–probe and holographic imaging experiments.

ACKNOWLEDGMENTS

The measurements were carried out at beamlines PG2, BL2, and BL3 at the FLASH facility at DESY, Hamburg. We would like to thank the scientific and technical staff at FLASH, especially A. Al-Shemary, H. Redlin, S. Düsterer, and R. Treusch, for their support.

Financial support in the Cluster of Excellence "Nanospintronics" funded by the Forschungs- und Wissenschaftsstiftung Hamburg, by BMBF under 05K10GU4/FSP-301, and by German Research Foundation (DFG) within SFB 668 and SFB 925 is gratefully acknowledged.

[1] E. Beaurepaire, J.-C. Merle, A. Daunois, and J.-Y. Bigot, Phys. Rev. Lett. **76**, 4250 (1996).
[2] E. Carpene, E. Mancini, C. Dallera, E. Puppin, and S. De Silvestri, Thin Solid Films **519**, 1642 (2010).
[3] L.-W. Kim, H.-S. Song, J.-W. Jeong, K.-D. Lee, J.-W. Sohn, T. Shima, and S.-C. Shin, Appl. Phys. Lett. **98**, 092509 (2011).
[4] J. Wang, C. Sun, Y. Hashimoto, J. Kono, G. A. Khodaparast, Ł. Cywiński, L. J. Sham, G. D. Sanders, C. J. Stanton, and H. Munekata, J. Phys.: Condens. Matter **18**, R501 (2006).
[5] A. Kirilyuk, A. V. Kimel, and T. Rasing, Rev. Mod. Phys. **82**, 2731 (2010).
[6] K. Vahaplar, A. M. Kalashnikova, A. V. Kimel, S. Gerlach, D. Hinzke, U. Nowak, R. Chantrell, A. Tsukamoto, A. Itoh, *et al.*, Phys. Rev. B **85**, 104402 (2012).
[7] R. W. Schoenlein, S. Chattopadhyay, H. H. W. Chong, T. E. Glover, P. A. Heimann, C. V. Shank, A. A. Zholents, and M. S. Zolotorev, Science **287**, 2237 (2000).
[8] B. T. Thole, P. Carra, F. Sette, and G. van der Laan, Phys. Rev. Lett. **68**, 1943 (1992).
[9] P. Carra, B. T. Thole, M. Altarelli, and X. Wang, Phys. Rev. Lett. **70**, 694 (1993).
[10] J. Stöhr and H. König, Phys. Rev. Lett. **75**, 3748 (1995).
[11] C. Boeglin, E. Beaurepaire, V. Halté, V. López-Flores, C. Stamm, N. Pontius, H. A. Dürr, and J.-Y. Bigot, Nature (London) **465**, 458 (2010).
[12] Y. Acremann, J. P. Strachan, V. Chembrolu, S. D. Andrews, T. Tyliszczak, J. A. Katine, M. J. Carey, B. M. Clemens, H. C. Siegmann, and J. Stöhr, Phys. Rev. Lett. **96**, 217202 (2006).
[13] S. Eisebitt, J. Lüning, W. F. Schlotter, M. Lörgen, O. Hellwig, W. Eberhard, and J. Stöhr, Nature (London) **432**, 885 (2004).
[14] D. Stickler, R. Frömter, H. Stillrich, C. Menk, C. Tieg, S. Streit-Nierobisch, M. Sprung, C. Gutt, L. M. Stadler, O. Leupold, *et al.*, Appl. Phys. Lett. **96**, 042501 (2010).
[15] E. Guehrs, C. M. Günther, B. Pfau, T. Rander, S. Schaffert, W. F. Schlotter, and S. Eisebitt, Opt. Express **18**, 18922 (2010).
[16] C. Gutt, L. M. Stadler, S. Streit-Nierobisch, A. P. Mancuso, A. Schropp, B. Pfau, C. M. Günther, R. Könnecke, J. Gulden, B. Reime, *et al.*, Phys. Rev. B **79**, 212406 (2009).
[17] C. Gutt, S. Streit-Nierobisch, L.-M. Stadler, B. Pfau, C. M. Günther, R. Könnecke, R. Frömter, A. Kobs, D. Stickler, H. P. Oepen, *et al.*, Phys. Rev. B **81**, 100401(R) (2010).
[18] E. Pedersoli, F. Capotondi, D. Cocco, M. Zangrando, B. Kaulich, R. H. Menk, A. Locatelli, T. O. Mentes, C. Spezzani, G. Sandrin, *et al.*, Rev. Sci. Instrum. **82**, 043711 (2011).
[19] W. F. Schlotter, J. J. Turner, M. Rowen, P. Heimann, M. Holmes, O. Krupin, M. Messerschmidt, S. Moeller, J. Krzywinski, R. Soufli, *et al.*, Rev. Sci. Instrum. **83**, 043107 (2012).
[20] T. Wang, D. Zhu, B. Wu, C. Graves, S. Schaffert, T. Rander, L. Mueller, B. Vodungbo, C. Baumier, D. P. Bernstein, *et al.*, Phys. Rev. Lett. **108**, 267403 (2012).
[21] B. Faatz, N. Baboi, V. Ayvazyan, V. Balandin, W. Decking, S. Duesterer, H. J. Eckoldt, J. Feldhaus, N. Golubeva, K. Honkavaara, *et al.*, Nucl. Instrum. Methods Phys. Res. A **635**, S2 (2011).
[22] M. Martins, M. Wellhöfer, J. T. Hoeft, and W. Wurth, Rev. Sci. Instrum. **77**, 115108 (2006).
[23] W. Ackermann, G. Asova, V. Ayvazyan, A. Azima, N. Baboi, J. Baehr, V. Balandin, B. Beutner, A. Brandt, A. Bolzmann, *et al.*, Nature Photon. **1**, 336 (2007).
[24] K. Tiedtke, A. Azima, N. von Bargen, L. Bittner, S. Bonfigt, S. Düsterer, B. Faatz, U. Fühling, M. Gensch, C. Gerth, *et al.*, New J. Phys. **11**, 023029 (2009).
[25] R. Treusch and J. Feldhaus, New J. Phys. **12**, 035015 (2010).
[26] H. Redlin, A. Al-Shemmary, A. Azima, N. Stojanovic, F. Tavella, I. Will, and S. Düsterer, Nucl. Instrum. Methods Phys. Res. A **635**, S88 (2011).
[27] B. L. Henke, E. M. Gullikson, and J. C. Davis, At. Data Nucl. Data Tables **54**, 181 (1993).
[28] P. Radcliffe, S. Düsterer, A. Azima, W. B. Li, E. Plönjes, H. Redlin, J. Feldhaus, P. Nicolosi, L. Poletto, J. Dardis, *et al.*, Nucl. Instrum. Methods Phys. Res. A **583**, 516 (2007).
[29] A. Azima, S. Düsterer, P. Redcliffe, H. Redlin, N. Stojanovic, W. Li, H. Schlarb, J. Feldhaus, D. Cubaynes, M. Meyer, *et al.*, Appl. Phys. Lett. **94**, 144102 (2009).
[30] P. Radcliffe, S. Düsterer, A. Azima, H. Redlin, J. Feldhaus, J. Dardis, K. Kavanagh, H. Luna, J. Pedregosa Gutierrez, P. Yeates, *et al.*, Appl. Phys. Lett. **90**, 131108 (2007).
[31] *Small Angle X-ray Scattering*, edited by O. Glatter and O. Kratky (Academic, 1982).
[32] J. P. Hannon, G. T. Trammell, M. Blume, and D. Gibbs, Phys. Rev. Lett. **61**, 1245 (1988).
[33] H. Ebert, R. Wienke, G. Schütz, and R. Zeller, J. Appl. Phys. **67**, 4923 (1990).
[34] G. Schütz, W. Wagner, W. Wilhelm, and P. Kienle, Phys. Rev. Lett. **58**, 737 (1987).
[35] J. Stöhr, J. Electron Spectrosc. Relat. Phenom. **75**, 253 (1995).
[36] J. Stöhr and H. C. Siegmann, *Magnetism, from Fundamentals to Nanoscale Dynamics* (Springer, 2006).
[37] S. Eisebitt, M. Lörgen, W. Eberhard, J. Lüning, J. Stöhr, C. T. Rettner, O. Hellwig, E. E. Fullerton, and G. P. Denbeaux, Phys. Rev. B **68**, 104419 (2003).
[38] H. Stillrich, C. Menk, R. Frömter, and H.-P. Oepen, J. Magn. Magn. Mater. **322**, 1353 (2010).
[39] M. Wellhöfer, M. Weißenborn, R. Anton, S. Pütter, and H.-P. Oepen, J. Magn. Magn. Mater. **292**, 345 (2005).
[40] J. B. Kortright, S.-K. Kim, G. P. Denbeaux, G. Zeltzer, K. Takano, and E. E. Fullerton, Phys. Rev. B **64**, 092401 (2001).
[41] O. Hellwig, A. Berger, J. B. Kortright, and E. E. Fullerton, J. Magn. Magn. Mater. **319**, 13 (2007).
[42] G. Grübel and F. Zontone, J. Alloys Compd. **362**, 3 (2004).
[43] G. Grübel, G. B. Stephenson, C. Gutt, H. Sinn, and T. Tschentscher, Nucl. Instrum. Methods Phys. Res. B **262**, 357 (2007).
[44] N. Del Fatti, C. Voisini, M. Achermann, S. Tzortzakis, D. Christofilos, and F. Valée, Phys. Rev. B **61**, 16956 (2000).

[45]E. Carpene, E. Mancini, C. Dallera, M. Brenna, E. Puppin, and S. De Silvestri, Phys. Rev. B **78**, 174422 (2008).
[46]M. Cinchetti, M. Sánchez Albandea, D. Hoffmann, T. Roth, J.-P. Wüstenberg, M. Krauß, O. Andreyev, H. C. Schneider, M. Bauer, and M. Aeschlimann, Phys. Rev. Lett. **97**, 177201 (2006).
[47]B. Pfau, S. Schaffert, L. Müller, C. Gutt, A. Al-Shemmary, F. Büttner, R. Delauny, S. Düsterer, S. Flewett, R. Frömter, *et al.*, Nat. Commun. **3**, 1100 (2012).
[48]K. M. Davis, K. Miura, N. Sugimoto, and K. Hirao, Opt. Lett. **21**, 1729 (1996).
[49]K. Miura, J. Qiu, H. Inoue, and T. Mitsuyo, Appl. Phys. Lett. **71**, 3329 (1997).
[50]V. R. Bhardwaj, E. Simova, P. B. Corkum, D. M. Rayner, C. Hnatovsky, R. S. Taylor, B. Schreder, M. Kluge, and J. Zimmer, J. Appl. Phys. **97**, 083102 (2005).
[51]E. N. Glezer, Y. Siegal, L. Huang, and E. Mazur, Phys. Rev. B **51**, 6959 (1995).
[52]A. M. Lindenberg, S. Engemann, K. J. Gaffney, K. Sokolowski-Tinten, J. Larsson, P. B. Hillyard, D. A. Reis, D. M. Fritz, J. Arthur, R. A. Akre, *et al.*, Phys. Rev. Lett. **100**, 135502 (2008).
[53]L. Müller, C. Gutt, B. Pfau, S. Schaffert, J. Geilhufe, F. Büttner, J. Mohanty, S. Flewett, R. Treusch, S. Düsterer, *et al.*, "Breakdown of the X-ray resonant magnetic scattering signal during intense XUV FEL irradiation," Phys. Rev. Lett. (submitted).
[54]B. Pfau, C. M. Günter, R. Könnecke, E. Guehrs, O. Hellwig, W. F. Schlotter, and S. Eisebitt, Opt. Express **18**, 13608 (2010).
[55]A. Bahrdt, W. Frentrup, A. Gaupp, B. Kuske, A. Meseck, and M. Scheer, in *Proceedings of the 2004 Free Electron Laser Conference* (BESSY, 2004), pp. 610–613.